

# Lawrence Berkeley National Laboratory

## LBL Publications

### Title

Characterization of Ordering in A-Site Deficient Perovskite  $\text{Ca}_{1-x}\text{La}_x\text{TiO}_3$  Using STEM/EELS

### Permalink

<https://escholarship.org/uc/item/88z7f1sw>

### Journal

Inorganic Chemistry, 55(19)

### ISSN

0020-1669

### Authors

Danaie, Mohsen  
Kepaptsoglou, Demie  
Ramasse, Quentin M  
et al.

### Publication Date

2016-10-03

### DOI

10.1021/acs.inorgchem.6b02087

Peer reviewed

## Characterization of Ordering in A-Site Deficient Perovskite $\text{Ca}_{1-x}\text{La}_{2x/3}\text{TiO}_3$ Using STEM/EELS

Mohsen Danaie,<sup>\*,†</sup> Demie Kepaptsoglou,<sup>‡</sup> Quentin M. Ramasse,<sup>‡</sup> Colin Ophus,<sup>§</sup> Karl R. Whittle,<sup>||,⊥</sup> Sebastian M. Lawson,<sup>||</sup> Stella Pedrazzini,<sup>†</sup> Neil P. Young,<sup>†</sup> Paul A. J. Bagot,<sup>†</sup> and Philip D. Edmondson<sup>#</sup>

<sup>†</sup>University of Oxford, Department of Materials, Parks Road, Oxford OX1 3PH, U.K.

<sup>‡</sup>SuperSTEM Laboratory, SciTech Daresbury Campus, Keckwick Ln, Warrington WA4 4AD, U.K.

<sup>§</sup>National Center for Electron Microscopy, Molecular Foundry, Lawrence Berkeley National Laboratory, 67 Cyclotron Road, Berkeley, California 94720, United States

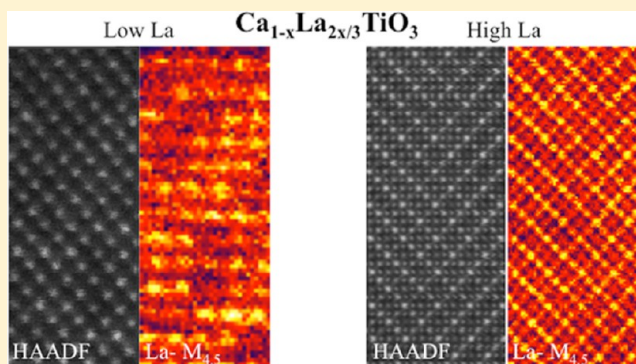
<sup>||</sup>University of Sheffield, Department of Materials Science & Engineering, Immobilisation Science Laboratory, Mappin Street, Sheffield S1 3JD, U.K.

<sup>⊥</sup>School of Engineering, University of Liverpool, Brownlow Hill, Liverpool L69 3GH, U.K.

<sup>#</sup>Materials Science & Technology Division, Oak Ridge National Laboratory, 1 Bethel Valley Road, Oak Ridge, Tennessee 37831, United States

### Supporting Information

**ABSTRACT:** The vacancy ordering behavior of an A-site deficient perovskite system,  $\text{Ca}_{1-x}\text{La}_{2x/3}\text{TiO}_3$ , was studied using atomic resolution scanning transmission electron microscopy (STEM) in conjunction with electron energy-loss spectroscopy (EELS), with the aim of determining the role of A-site composition changes. At low La content ( $x = 0.2$ ), adopting  $Pbnm$  symmetry, there was no indication of long-range ordering. Domains, with clear boundaries, were observed in bright-field (BF) imaging, but were not immediately visible in the corresponding high-angle annular dark-field (HAADF) image. These boundaries, with the aid of displacement maps from A-site cations in the HAADF signal, are shown to be tilt boundaries. At the La-rich end of the composition ( $x = 0.9$ ), adopting  $Cmmm$  symmetry, long-range ordering of vacancies and  $\text{La}^{3+}$  ions was observed, with alternating La-rich and La-poor layers on  $(001)_p$  planes, creating a double perovskite lattice along the  $c$  axis. These highly ordered domains can be found isolated within a random distribution of vacancies/ $\text{La}^{3+}$ , or within a large population, encompassing a large volume. In regions with a high number density of double perovskite domains, these highly ordered domains were separated by twin boundaries, with  $90^\circ$  or  $180^\circ$  lattice rotations across boundaries. The occurrence and characteristics of these ordered structures are discussed and compared with similar perovskite systems.



## 1. INTRODUCTION

Perovskite structures based on the formulation  $\text{Ca}_{1-x}\text{La}_{2x/3}\text{TiO}_3$  have been studied extensively for use across a wide range of possible applications, such as anodes for solid oxide fuel cells (SOFCs),<sup>1</sup> as dielectric resonators,<sup>2</sup> as high-density memory storage devices,<sup>3</sup> as host matrices for inert matrix nuclear fuels, and as containment media for high-level nuclear waste forms.<sup>4–6</sup> Understanding the crystallographic ordering at the atomic scale and the nature of defects is essential in order to successfully utilize this class of perovskites across the multitude of applications.

The crystal structure of  $\text{CaTiO}_3$  at room temperature is known to be orthorhombic, adopting  $Pbnm$  symmetry, similar to  $\text{GdFeO}_3$ .<sup>7</sup> On heating, there are two phase transitions: first to tetragonal  $I4/mcm$  at 1523 K and cubic  $Pm-3m$  at 1647 K.<sup>7</sup> The high-temperature cubic phase adopts the prototypical

perovskite structure,  $\text{ABO}_3$ , with B cations within  $\text{BO}_6$  octahedral units and A cations at the center of a cube with cuboctahedral coordination with O ions, i.e.  $\text{AO}_{12}$ . In contrast, the structures found at lower temperatures have lower symmetry, corresponding to changes in  $\text{BO}_6$  octahedral tilting, distortions in octahedral spaces, or off-center B cation.<sup>8</sup> Using Glazer notation,<sup>9</sup> widely used to represent tilts in octahedra within perovskite structures, the high-temperature structure is  $a^0a^0a^0$ , whereas  $I4/mcm$  is  $a^0a^0c^-$ , and  $Pbnm$  is  $a^-a^-c^+$ .

As this paper concerns the structural characterization of  $\text{Ca}_{1-x}\text{La}_{2x/3}\text{TiO}_3$ , it is instructive to probe the existing literature on the other end member of this compound perovskite as well, i.e.  $\text{La}_{2/3}\text{TiO}_3$ . The formation of A-site deficient perovskite in

Received: August 30, 2016

Published: September 15, 2016

the La–Ti–O system, with Ti in the +4 oxidation state, was first reported by Kestigian and Ward.<sup>10</sup> [With Ti in the purely +3 oxidation state, LaTiO<sub>3</sub> is formed with *Pbmm* symmetry, with  $a = 5.63$  Å,  $b = 5.61$  Å, and  $c = 7.94$  Å.<sup>11,12</sup>] Abe and Uchino were the first to synthesize La<sub>2/3</sub>TiO<sub>3-λ</sub> as a single phase, with the suggested ionic arrangement of La<sub>2/3</sub><sup>3+</sup>Ti<sub>1-2λ</sub><sup>4+</sup>Ti<sub>2λ</sub><sup>3+</sup>Ti<sub>3-λ</sub><sup>2+</sup> and demonstrating with XRD that with a small amount of O deficiency ( $\lambda = 0.007$ ) the {002} line is split into three peaks. This is interpreted as doubling of the unit cell along the *c*-axis, resulting from a more facile formation of the perovskite phase with vacancy ordering on the A-sites.<sup>13</sup> Critical in attracting attention to this system was the report of high ionic conductivity in Li<sub>0.34</sub>La<sub>0.51</sub>TiO<sub>2.94</sub>, due to a large number of available vacant sites to diffusing Li ions.<sup>14</sup> Other studies report that pure La<sub>2/3</sub>TiO<sub>3</sub> (also written as La<sub>2</sub>Ti<sub>3</sub>O<sub>9</sub>) could not be stabilized,<sup>15,16</sup> or have indexed this structure as tetragonal (*I4/mmm*) with  $a = b = 3.856$  Å, and  $c = 24.6$  Å.<sup>17</sup> The latter structure corresponds to a layered ordering configuration along [001]<sub>p</sub> with 2 layers filled and one layer vacant A-sites, hence the relatively large *c* axis for this unit cell.

Previous structure determinations of Ca<sub>1-x</sub>La<sub>2x/3</sub>TiO<sub>3</sub> perovskites have used X-ray and neutron diffraction. Vashook et al.<sup>1</sup> examined the phase transitions within the Ca<sub>1-x</sub>La<sub>2x/3</sub>TiO<sub>3</sub> series using X-ray diffraction, showing that for the Ca-rich composition ( $x = 0.2$ ) the structure adopted *Pbmm* symmetry, changing to a body-centered orthorhombic symmetry (*Imma*) at  $x = 0.4$ . At the La-rich composition ( $x = 0.9$ ) two structures were equally possible, monoclinic (*P2/m*) and orthorhombic (*Cm2m*). Vashook et al.<sup>1</sup> highlighted the peculiarity of the La(Ca) cation ordering and the A-site vacancies in La<sub>0.6</sub>Ca<sub>0.1</sub>TiO<sub>3</sub>, which were absent in both La<sub>0.13</sub>Ca<sub>0.8</sub>TiO<sub>3</sub> and La<sub>0.4</sub>Ca<sub>0.4</sub>TiO<sub>3</sub>. More recently,<sup>18</sup> using synchrotron X-rays, the symmetries in Ca<sub>1-x</sub>La<sub>2x/3</sub>TiO<sub>3</sub> were identified as *Pbmm* ( $x = 0.0–0.3$ ), *Imma* ( $x = 0.4–0.6$ ), *I4/mcm* ( $x = 0.7–0.75$ ), and finally *Cmmm* for the La-rich extreme case ( $x = 0.8–0.98$ ). For this La-rich phase, an ordered perovskite structure with alternating fully and partially (40%) occupied layers of A-site cations was observed. Zhang et al.<sup>19</sup> combined neutron and synchrotron X-ray structural refinements on nominally the same system, showing the following phase stability regions:

- (i)  $0 \leq x \leq 0.5$ ; *Pbmm* symmetry
- (ii)  $0.5 < x < 0.7$ ; *Ibmm* symmetry
- (iii)  $0.7 \leq x < 0.9$ ; *I4/mcm* symmetry
- (iv)  $x \geq 0.9$ ; *Cmmm*, with long-range ordering found at  $x = 0.9$

While these techniques provide atomic scale information on both the unit cell and lattice, they are averaged over the entire volume examined. As such, they can be less sensitive to atomic scale segregation or ordering within the lattice. Aberration-corrected scanning transmission electron microscopy (STEM) in conjunction with electron energy-loss spectroscopy (EELS), provides an alternative approach to resolve atomic-scale segregation and/or ordering in such systems.

Table 1 presents an overview of the space groups occurring in the CLTO system across the full-range of composition, using data provided by Zhang et al.<sup>19</sup> The TiO<sub>6</sub> octahedra tilts in each case are shown in the crystal models, also provided in Glazer's notation in the third column.<sup>19,20</sup> In the case of the *Cmmm* space group, besides the tilt in octahedra, there is significant displacement of the B-site cation (Ti) within the octahedral space (the difference between maximum and minimum Ti–O bond lengths accounts for 9.66%), concurrent with distortions

**Table 1. Crystal Structures Reported<sup>11</sup> in the CLTO System along the Pseudocubic Directions [001]<sub>p</sub> and [100]<sub>p</sub><sup>a</sup>**

Space group	Projection along [001] <sub>p</sub>	Projection along [100] <sub>p</sub>	Unit Cell Tilt system (Glazer notation)
<i>Pbmm</i>			$a = a_p\sqrt{2}$ $b = b_p\sqrt{2}$ $c = 2c_p$ $a^-a^-c^+$
<i>Ibmm</i>			$a = a_p\sqrt{2}$ $b = b_p\sqrt{2}$ $c = 2c_p$ $a^-a^-c^0$
<i>I4/mcm</i>			$a = b = a_p\sqrt{2}$ $c = 2c_p$ $a^0a^0c^-$
<i>Cmmm</i>			$a = 2a_p$ $b = 2b_p$ $c = 2c_p$ $a^-b^0c^0$

<sup>a</sup>The third column provides the relationships between the pseudocubic and actual unit cells and the octahedra tilt system (in Glazer notation). [Colour scheme: Ti orange, O red, Ca blue, and La green].

in the TiO<sub>6</sub> octahedral space, i.e. ~5.5% of the maximum O–O bond length disparity. There are small distortions present in the B-site within the other space groups, but the Ti–O bond length differences are very small (<0.7%) and, at least in the context of the present study, can be ignored.

In the present study we performed detailed atomic scale characterization using scanning transmission electron microscopy concurrent with electron energy-loss spectroscopy (STEM/EELS), taking advantage of the different modes of STEM high-resolution imaging and spectroscopy, and through computational electron microscopy. Using this approach, we elucidate the localized characteristics of ordering within the Ca<sub>1-x</sub>La<sub>2x/3</sub>TiO<sub>3</sub> system, with variation in *x*, and identify a high number density of various types of tilt boundaries. These atomic scale features are inaccessible in volume-averaged X-ray or neutron diffraction experiments performed in the past,<sup>19</sup> upon which we are building up the present investigation.

## 2. EXPERIMENTAL SECTION

The Ca<sub>1-x</sub>La<sub>2x/3</sub>TiO<sub>3</sub> specimens ( $x = 0.0, 0.1, \dots, 0.9$ ) were prepared by solid-state calcination of mixed oxides. Stoichiometric amounts of La<sub>2</sub>O<sub>3</sub> (Alfa Aesar 99.99%), were dried at 1073 K for 24 h, TiO<sub>2</sub> (Sigma-Aldrich ≥99%) and CaCO<sub>3</sub> (Alfa Aesar 99.5%) were dried at 453 K for 24 h, prior to weighing, then all were milled with isopropanol in a planetary ball-mill. Once dried, the powders were sieved, pressed into pellets, and heated to 1573 K in air for 24 h, with a ramp rate of 5 K min<sup>-1</sup>. Following this, they were reground, sieved, and pressed once more before sintering at 1673 K in air for a further 48 h, achieving a relative sample density of >95% of the theoretical value, determined via the Archimedes method. The final pellets were

ground with silicon carbide and polished to a 1  $\mu\text{m}$  finish with diamond suspension (MatPrep) prior to thermal etching at 1523 K for 2 h in air. X-ray diffraction patterns were recorded using a STOE STADI P image plate diffractometer with a  $\text{Cu K}\alpha 1$  ( $\lambda = 1.5406 \text{ \AA}$ ) beam, at 40 kV, 35 mA. The patterns were collected between  $0^\circ$  and  $100^\circ$  with an integrated step size of  $0.03^\circ$  and an average counting time of 1 s per point. The alignment was checked using an independent silicon calibration run.

Samples for transmission electron microscopy were prepared both using the focused-ion beam (FIB) lift-out technique<sup>21</sup> (Zeiss-NVision 40) and by grinding the pellets into electron-transparent particles, subsequently suspended in high-purity chloroform, dispersed onto a gold-supported lacey carbon network (Agar Lacey carbon film, H7 Au), and then dried in air. Samples prepared via FIB lift-out were initially coated with a thin layer of gold for better conductivity. To ensure minimal Ga-beam damage, the TEM lamellae were polished with gradually decreasing beam accelerating voltage and current, with a final cleaning done with a 2 kV Ga beam. All samples were stored under vacuum after preparation.

Preliminary TEM characterization was performed using a JEOL 2100 microscope, operated at accelerating voltages of 80 kV and at 200 kV. The lower voltage was aimed at screening suitable regions for subsequent STEM/EELS analysis. STEM/EELS analysis was performed using a Nion UltraSTEM 100 dedicated ultrahigh-vacuum scanning transmission electron microscope, equipped with a Gatan Enfina EELS spectrometer (SuperSTEM, Daresbury) operated at 100 kV accelerating voltage, with  $\sim 0.3 \text{ eV}$  native energy resolution, measured at full-width at half-maximum of the zero-loss peak. The effective energy resolution for the experiments was limited by the spectrometer detector point spread function, which is dependent on the dispersion chosen. The probe-forming optics were adjusted to provide a beam of  $\sim 100 \text{ pA}$  with a convergence semiangle of  $32 \text{ mrad}$ , corresponding to a  $0.9 \text{ \AA}$  probe size. The high-angle annular dark-field detector used to record the images had a semiangular range of  $85\text{--}190 \text{ mrad}$ , while the bright-field detector covered a semiangular range of  $3.4 \text{ mrad}$ ; annular bright-field (ABF) images were also acquired, with a detector adjusted to cover a semiangular range of  $15\text{--}32 \text{ mrad}$ . At these settings, a second annular detector can record simultaneously a low-angle annular dark-field (LAADF) signal over a  $35\text{--}190 \text{ mrad}$  semiangular range. Energy loss spectra were acquired using a collection semiangle of  $36 \text{ mrad}$ . High-angle annular dark-field (HAADF) and bright-field (BF) images were acquired simultaneously. The BF signal is largely dominated by phase contrast (similar to high-resolution TEM imaging by the reciprocity principle), whereas the HAADF signal is largely due to thermal diffuse scattering; hence, it is incoherent and sensitive to atomic number ( $Z$ ).<sup>22</sup> These two imaging signals are complementary in detecting variations in the octahedral tilting (BF<sup>23,24</sup> and ABF<sup>25</sup>) versus the distribution of heavier elements, i.e. Ti, Ca, and La (HAADF). As a rule of thumb, in order for the ADF image to be interpretable as  $Z$ -contrast, the inner collection angle of the detector has to be around three times the probe half angle.<sup>26</sup> With the angular values stated as above, this is satisfied for the HAADF signal presented.

For simulation of the selected area diffraction patterns, the JEMS software was used.<sup>27</sup> Throughout this paper, unless specified, plane/orientation indices are provided with respect to the pseudocubic unit cell, emphasized with the subscript "p". To perform accurate image analysis on STEM micrographs, two techniques were utilized to enhance signal-to-noise ratio: (i) fast (typically  $5 \mu\text{s}$  per pixel) acquisition of multiple frames, which were then aligned and summed using the Digital Micrograph software suite, and (ii) nonlinear drift correction using  $0^\circ$  and  $90^\circ$  scan rotation pairs acquired at slower rates (typically  $150 \mu\text{s}$  per pixel).<sup>28</sup> For a number of drift-corrected data sets, using a peak-finding algorithm implemented in a MATLAB code, where a five-parameter Gaussian function was fitted to the peak positions, mean "unit cells" were constructed by averaging along an axis of interest in the HAADF images. These were then utilized to plot displacement maps of the cations along different zone axes. Multislice STEM image simulations with 8 frozen phonon configurations were performed with custom written Matlab code, using the methods and

potentials outlined by E. J. Kirkland.<sup>29</sup> Simulation parameters were set to match the experimental conditions.

### 3. RESULTS

**3-1. X-ray Diffraction.** X-ray diffraction patterns across the compositional range of the as-prepared  $\text{Ca}_{1-x}\text{La}_{2x/3}\text{TiO}_3$  system are shown in Figure 1. All plots were normalized to the peak

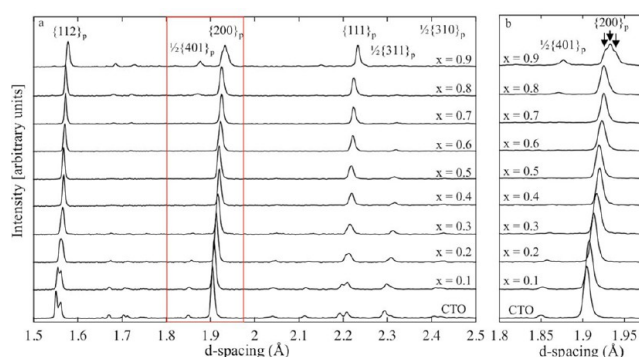


**Figure 1.** (a) X-ray diffraction data for the complete composition range in the CLTO ( $\text{Ca}_{1-x}\text{La}_{2x/3}\text{TiO}_3$ ) system. Indices are provided with respect to the pseudocubic cell. Plot in (b) shows the details of the  $\{200\}_p$  peak. Diffractograms are normalized with respect to the  $\{110\}_p$  peak intensity and shifted in the  $y$ -direction for better visibility.

intensity for the  $\{110\}_p$  pseudocubic reflection, the strongest reflection in all cases. It can be seen that the main pseudocubic reflections shift toward larger  $d$ -spacing values with increasing La content. This can be attributed to the slightly larger size of the  $\text{La}^{3+}$  ion (electronic structure of La is  $[\text{Xe}] 5d^1 6s^2$ , rarely adopting oxidation states other than  $3+$ )<sup>30</sup> compared to  $\text{Ca}^{2+}$  ( $117.2 \text{ pm}$  versus  $114 \text{ pm}$ ).<sup>31</sup> This shift agrees with the neutron diffraction analysis performed by Zhang et al.<sup>19</sup> Using X-ray diffraction alone, it is difficult to determine the composition at which the transition from  $Pbnm$  ( $a^-a^-c^+$ ) to  $Ibmm$  ( $a^-a^-c^0$ ), i.e. the disappearance of the  $1/2\{310\}$  peak corresponding to the in-phase  $c^+$  tilt,<sup>32</sup> occurs. In contrast, using neutron diffraction, it is clear this takes place at  $x = 0.6$  CLTO composition.<sup>19</sup>

Given the limitations of X-ray diffraction, it is difficult to definitively ascertain the formation of the  $Ibmm$  and the  $I4/mcm$  space groups. In contrast, the formation of the  $Cmmm$  space group by  $x = 0.9$  is evident in our data. This is highlighted by the splitting of the  $\{200\}_p$  peak into a triplet, Figure 1(b), suggesting a transition to orthorhombic symmetry, coupled with the emergence of a peak at  $1/2\{401\}_p$ . The tilt system for  $Cmmm$  is  $a^-b^0c^0$ , so we expect to see a reflection at  $1/2\{311\}$ ,<sup>32</sup> as also seen using neutron diffraction.<sup>19</sup> The data here shows the peak at  $1/2\{311\}$  strongly present in the  $Pbnm$  ( $a^-a^-c^+$ ) space group, but gradually diminishing at higher  $x$  values. This is likely to arise from the different scattering parameters for X-rays and neutrons. The peak at  $1/2\{401\}$ , given the tilt system of  $a^-b^0c^0$  for this space group, would not normally be expected to be associated with octahedral tilting and most likely corresponds to an off-center Ti position within the octahedron.

As the presence of the  $Ibmm$  and  $I4/mcm$  symmetries could not be confirmed by XRD, TEM characterization was limited to those that could, i.e.  $Pbnm$  and  $Cmmm$ . Given the narrow stability region for  $Ibmm$  and  $I4/mcm$  symmetries, it is possible that, for compositions  $x = 0.6$  to  $0.8$ , there is a mixture of phases. Hence, we will focus on the extreme cases of La-lean

( $Pbnm$ ) and La-rich ( $Cmmm$ ) space groups for electron microscopy characterization.

**3-2. Electron Microscopy Characterization—CLTO with Low La Content ( $x = 0.1$ – $0.5$ ).** Low magnification TEM observations of the low La-content CLTO samples reveal relatively large ( $>0.5 \mu\text{m}$  in size) domains separated with wide defect structures. Figure 2 shows the case for  $x = 0.1$  CLTO

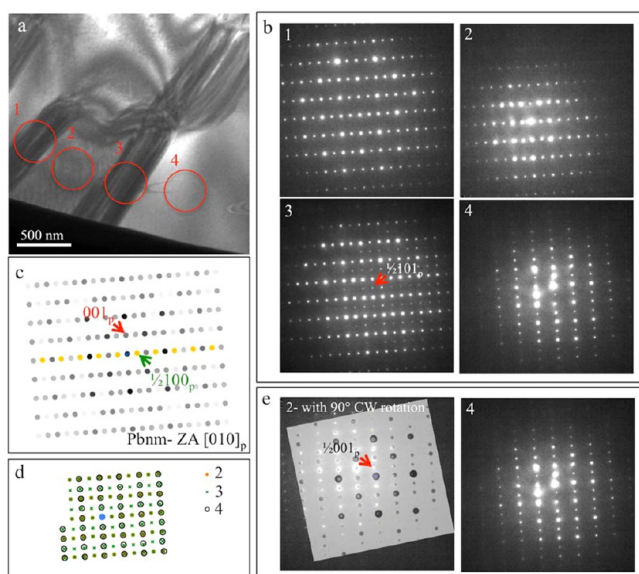


**Figure 2.** CLTO  $x = 0.1$  specimen (prepared via FIB) (a) showing the BF micrograph with bands of defects, across which selected area diffraction patterns were acquired. Areas marked in (a) correspond to the numbered diffraction patterns in (b). The zone axis is along  $[010]_p$  of the pseudocubic lattice (or  $110$  of the  $Pbnm$  orthorhombic unit cell). The simulation in (c) is the dynamical diffraction pattern assuming  $200 \text{ nm}$  thickness and the reported crystallographic parameters in Zhang et al. The colored spots show potential for double diffraction. (d) Schematic of diffraction peak positions in data sets 2, 3, and 4. (e) Compares diffraction (2) with  $90^\circ$  CW rotation with pattern (4).

using a FIB-prepared sample. A series of selected area diffraction patterns were acquired across the region shown in Figure 2(a), with the numbered circles indicating the regions corresponding to the experimental electron diffraction patterns, presented in Figure 2(b). In pattern 1, there is a good match with the simulated kinematical pattern (using the structure reported by Zhang et al.<sup>19</sup>), with the reflection at  $1/2100_p$  present. Pattern 2 shows a similar configuration, whereas in pattern 3 the coexistence of  $1/2100_p$ ,  $1/2101_p$ , and  $1/2001_p$  is observed. In pattern 4, if the same zone axis and in-plane orientation is assumed,  $1/2001_p$  gains intensity whereas  $1/2100_p$  vanishes. From this, we infer that the reflection observed at  $1/2100_p$  cannot be due to double diffraction, as in that case it would be expected to exist across all patterns. Furthermore, close inspection of patterns 2 and 4 indicates that they differ through a  $90^\circ$  rotation, demonstrated in Figure 2(c).

From prior neutron diffraction analysis,<sup>19</sup> it is known that the  $Pbnm$  symmetry within the CLTO system corresponds to a  $a^-c^+$  tilting. Woodward and Reaney<sup>32</sup> suggest this gives rise to the presence of  $1/2(eeo)$  reflections (e: even; o: odd) on  $[100]$  or  $[010]$  zone axis patterns. Since this is a mix of in-phase and antiphase tilts, we can expect to observe  $1/2\{oeo\}$  reflections; however, these reflections can also indicate

antiparallel cation displacement. Hence, the presence of  $1/2001_p$  and  $1/2101_p$  can correlate to mixed octahedral tilting. The presence of  $1/2100_p$  in patterns 1 and 2 seems to be an outlier, which could be resolved by indexing these two patterns in the same zone axis but with a  $90^\circ$  in-plane rotation, Figure 2(c). This suggests that, in the region shown, when passing across the band highlighted in #3, the crystal rotates  $90^\circ$ ; that is, the region in #3 is a  $90^\circ[010]_p$  tilt boundary, with the beam incident along the tilt axis. Note that the diffraction peaks in #3 can be accounted for by superimposing the two patterns in #2 and #4, except the  $1/2101_p$  peaks (See schematic in panel (d)). It is possible that this boundary in #3 is inclined to the incident electron beam. In that case, it is expected to merely observe superposition of patterns from the adjoining grains in the region of the boundary. The presence of the  $1/2101_p$  peaks seems to reject this scenario. The appearance of this reflection suggests a mechanism that accommodates changes in tilt directions of the octahedra. From a broader perspective, it can be seen that the tilting of the  $\text{TiO}_6$  octahedra is clearly not the same across the bulk with regions separated by transition bands/defects. A similar observation of such lattice tilt rotation in  $x = 0.1$  CLTO is presented in Figure S1 in the Supporting Information.

In order to examine different zone axes, crushed powder samples were prepared and Figure 3 shows high-resolution images from  $x = 0.2$  with the electron beam incident along the  $[010]_p$  direction (Similar to Figure 2). Pairs of HAADF/BF STEM micrographs are shown in panels (a) and (b), with a low magnification image of the particle included as an insert in (a) (a selected area diffraction pattern collected at low magnification is presented in the Supporting Information, Figure S2). The variations in intensity in HAADF images correspond to varying distributions of La versus Ca in A-site positions, with La-rich columns appearing brighter in intensity. Atomically resolved core-loss electron energy-loss spectra were gathered along this zone axis to directly map the distribution of Ca versus La-rich columns. The area marked in the HAADF micrograph in Figure 3(c), acquired along the same zone axis as above—with only a scan rotation, is representative of such EELS measurements. The sum of the electron energy-loss spectrum across the entire spectrum image area, Figure 3(d), shows the characteristic Ca- $L_{2,3}$ , Ti- $L_{2,3}$ , O-K, and La- $M_{4,5}$  excitation edges. In Figure 3(e), along with the HAADF signal gathered during the spectrum image acquisition, elemental intensity maps, after background subtraction, are shown. The intensity maps of Ca and La in panel (e) show their respective distributions on the A-site, with high occupancy of one species resulting in lower intensity of the other. Domain boundaries, previously observed in Figure 2, were not encountered during high-magnification STEM/EELS examination along this zone axis. Given the large size and low number density of such domains, this is not surprising.

Other boundaries indicating octahedral tilting were nevertheless observed at other zone axes, as described later in this section.

The  $x = 0.2$  CLTO perovskite along the  $[001]_p$  zone axis was examined across different particles (Figures 4 and 5). In Figure 4, the HAADF signal again shows variations in intensity, due to variations in La/Ca and A-site vacancy distribution. The concurrently acquired BF signal, panel (b), shows a single domain, indicating no alteration in octahedral tilting within this region. Multislice simulations of expected HAADF and BF images, shown as lower insets in both panels, show a close

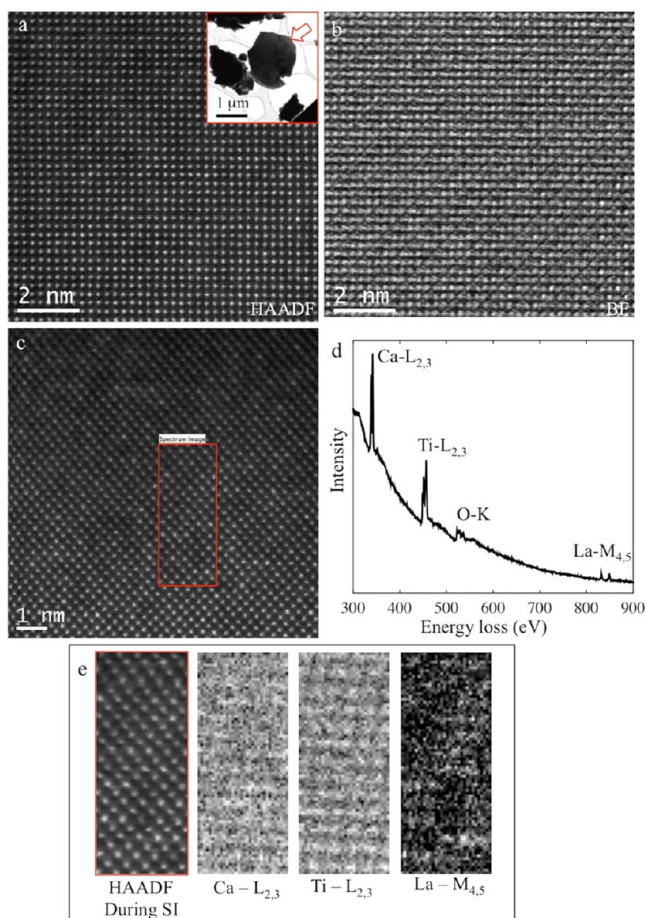


**Figure 3.** CLTO  $x = 0.2$  specimen (crushed grain sample) viewed along  $[010]_p$  ZA—the low magnification image of the particle used for these data sets is included as the inset in (a) the HAADF image. (b) BF signal acquired simultaneously with (a). (c) HAADF image close to the area in (a) with applied scan rotation. The region in the red frame was selected for EELS spectrum imaging. (d) EELS sum spectrum of the region in (c). (e) HAADF during SI acquisition image along with elemental intensity maps.

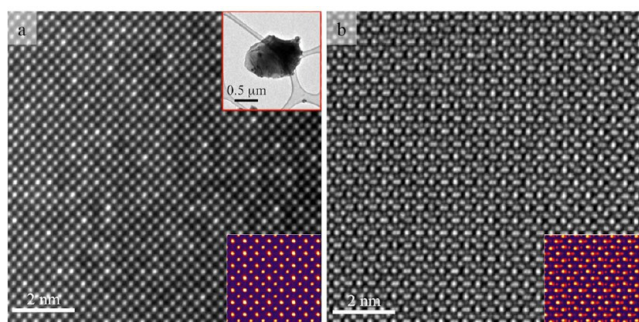


**Figure 4.** CLTO  $x = 0.2$  specimen (crushed grain sample) viewed along the  $[001]_p$  zone axis—the low magnification image of the particle used is shown as the upper inset in (a). (a) HAADF and (b) BF signal pairs acquired simultaneously. Lower insets are multislice simulations of HAADF and BF signals with 4 mrad probe tilt at 20 unit cells crystal thickness. An array of simulations for the BF signal, with changes in crystal thickness and probe tilt, is presented in the Supporting Information.

match at a crystal thickness of 20 unit cells. The contrast observed in BF could only be reproduced assuming a small tilt

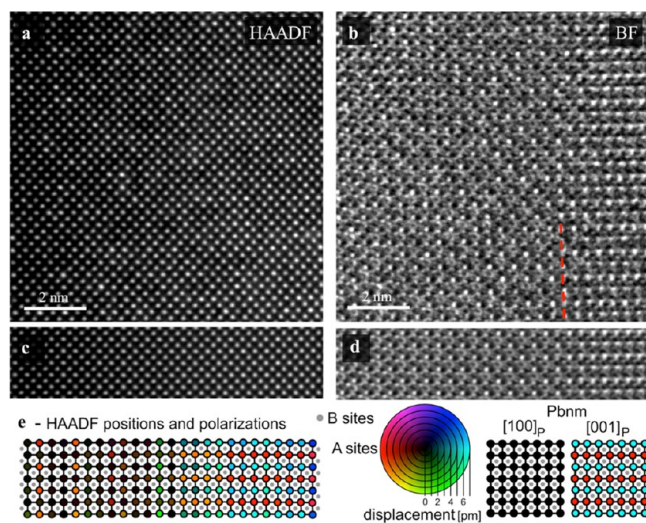


**Figure 5.** CLTO  $x = 0.2$  specimen (crushed grain sample) along  $[001]_p$  zone axis: (a) HAADF, (b) BF signals acquired simultaneously. (c and d) “unit cells” averaged along the vertical axes of images (a) and (b), respectively. (e) positions and displacements in A and B atomic sites, determined using the HAADF signal. The legend is provided on the right (B sites appear as gray; A sites are colored according to the magnitude and direction of displacement), with ideal atomic positions for  $[001]_p$  and  $[100]_p$  projections. The dashed line in (b) roughly marks the location of the boundary.

in the electron probe with respect to the sample, possibly due to local sample bending (here the case for 4 mrad tilt is presented). We recognize that the fit between the simulated and experimental BF is not ideal. This is due to the small size of the BF detector (3.4 mrad half-angle) compared to the probe convergence semiangle (32 mrad), potentially resulting in misalignment. Nevertheless, we can show that the elongated features in the BF image can result from beam tilt. A matrix of BF and HAADF image simulations with varying sample thickness and probe tilts is shown in Figure S4 in the Supporting Information. The HAADF signal was not as affected by the probe tilt compared to the BF signal. In fact, several publications, e.g. Yamazaki et al.,<sup>33</sup> have previously shown that crystal tilt does not significantly move peak intensities in HAADF, and just alters their relative intensities.

In Figure 5, projecting along a similar zone axis but from a different particle, a generally similar HAADF contrast is observed, panel (a); however, the simultaneously acquired BF signal, panel (b), shows domains. These domains, as they only appear in the BF image, can be related to changes in the tilt orientation of the  $\text{TiO}_6$  octahedra. Using the routine described in the Experimental Section, mean “unit cells” were constructed by averaging along the vertical axes of the HAADF and BF images, shown in panels (c) and (d). Since the variance in peak intensity for the B-sites (Ti) is much lower compared to the shared A-sites (Ca/La), these two positions could be readily identified after applying the peak-finding routine. Using a matrix of fitted peak positions from the HAADF signal, the deviation from the mean position can be mapped across the image, panel (e). The A-sites are colored according to the provided legend on the right-hand side, depending on the magnitude and the direction of displacement, relative to the neighboring B-sites. The B-site positions (shown in smaller gray circles) were not included in the displacement map. The nominal displacement of the A-sites along the  $[100]_p$  and

$[001]_p$  directions is also shown. The boundary evident in the BF signal coincides with the change in A-site displacement, as measured from the HAADF image. On the right section of the displacement map in panel (e) the displacement matches closely the nominal configuration along  $[001]_p$ . On the opposite side of the boundary, however, this configuration is completely changed, appearing closer to the  $[100]_p$  configuration, indicating a  $90^\circ[010]_p$  tilt boundary.

To highlight the changes in octahedral tilts, STEM measurements along the  $[110]_p$  zone axis were undertaken, as shown in Figure 6. Along this axis, similar boundaries—with

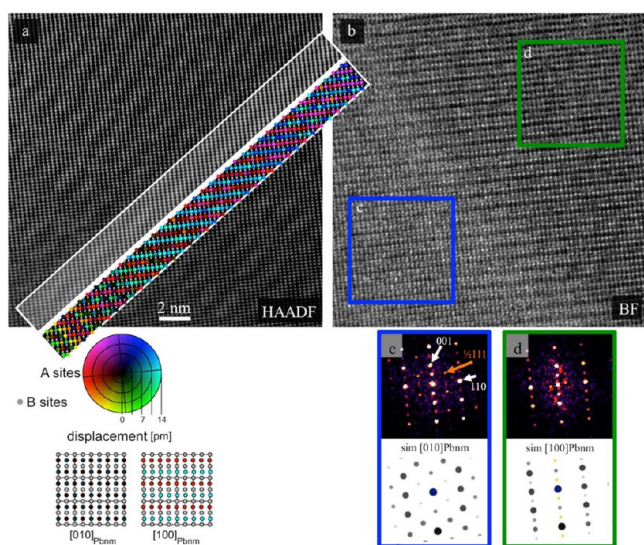


**Figure 6.** CLTO  $x = 0.2$  along the  $[110]_p$  zone axis: (a) HAADF and (b) BF images acquired simultaneously. The window over panel (a) contains both the averaged unit cell (measured along the shown direction from the HAADF image) and the A-site displacement map (B-sites appear as gray). Below panel (a) a legend for the map is provided, along with nominal displacement states along the  $[010]_{Pbnm}$  and  $[100]_{Pbnm}$  directions. Frames in (b) mark the locations corresponding to fast Fourier transforms in panels (c) and (d), respectively. In each case, a diffraction simulation is presented. (The low magnification image of the particle used and the corresponding SAD is shown in Figure S5.)

pronounced presence in BF, panel (b) in Figure 6, as opposed to a less obvious presence in the HAADF signal, panel (a)—were observed. Windowed Fast Fourier transformations (FFT) of the marked areas in (b) are shown in panels (c) and (d). The differences between the two FFTs are the presence of the  $1/2111_p$  spot in (c) (marked with arrow) and its absence in (d). This can be explained by indexing the FFT in (c) as the  $[010]_{Pbnm}$  zone axis and the FFT in (d) as  $[100]_{Pbnm}$  (Note that these would correspond to the  $[110]_p/[-110]_p$  directions in a pseudocubic cell). Simulations of diffraction patterns along those two zone axes are shown in panels (c) and (d) for clarity. In the case of  $[010]_{Pbnm}$ , the mixed tilt system ( $a^-a^-c^+$ ) gives rise to the appearance of the  $1/2111_p$  reflection. Crystal models along the two directions are presented in both cases, signifying that the atomic positions, aside from the  $O^{2-}$  ions, are very similar. This provides an explanation for the observed HAADF signal, showing only one single domain in Figure 6(a), since this signal is not affected by the  $O^{2-}$  ions. Superimposed on the HAADF micrograph (panel (a)) is the averaged unit cell, along with the A-site displacement map, with the legend provided.

The upper right corner of the image matches closely in A-site displacement with the nominal  $Pbnm$  configuration along the  $[100]_{Pbnm}$  zone axis (note the ideal crystal structure shown below). However, in the lower left section we observe a more random displacement, in-line with the  $[010]_{Pbnm}$  zone axis. This agrees with the observation from the FFT of the BF signal, as shown in panels (c) and (d). Given the above, the boundary observed in the BF signal, panel (b), comprises a tilt boundary with  $90^\circ$  rotation around the  $[001]_p$  axis, i.e.  $90^\circ[001]_p$ , imaged with the electron beam incident perpendicular to the tilt axis.

**3-3. Electron Microscopy Characterization—CLTO with High La Content ( $x = 0.9$ ).** For the La-rich CLTO sample ( $x = 0.9$ ), X-ray diffraction identified the structure as orthorhombic, adopting  $Cmmm$  symmetry. Figure 7(a) presents

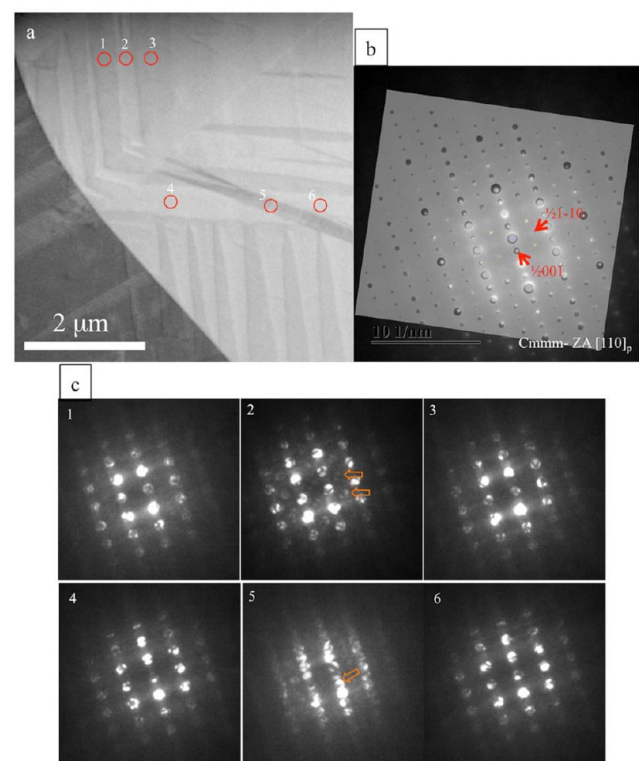


**Figure 7.** CLTO  $x = 0.9$  specimen (prepared by FIB) (a) low magnification STEM-DF image. The parallel beam diffraction pattern in (b) is acquired in TEM mode (at the same sample tilting conditions) from the right-hand side “grain” in (a). The red circles in (a) mark the spots used for CBED observations shown in (c). TEM bright-field image of the same region in (a) is presented in Figure S6 in the Supporting Information.

a low magnification STEM-DF image from such a composition, prepared via the FIB lift-out procedure. The orientation of the grain on the right-hand side of the image was adjusted in parallel beam illumination (TEM) mode to be along the  $[110]_p$  zone axis. The TEM-BF image taken from the same zone axis is presented in the Supporting Information (Figure S6). The corresponding selected area diffraction pattern, along with a simulation, is shown in panel (b). It can be observed here that the  $1/2001$ ,  $1/21-10$ , and  $1/21-11$  peaks are also present in this pattern. Each grain, as evident in panel (a), consists of twin-like domains. Since the small size of these domains made it difficult to capture isolated electron diffraction patterns in TEM mode, we acquired small convergence angle electron diffraction (CBED) patterns in STEM mode instead, which has

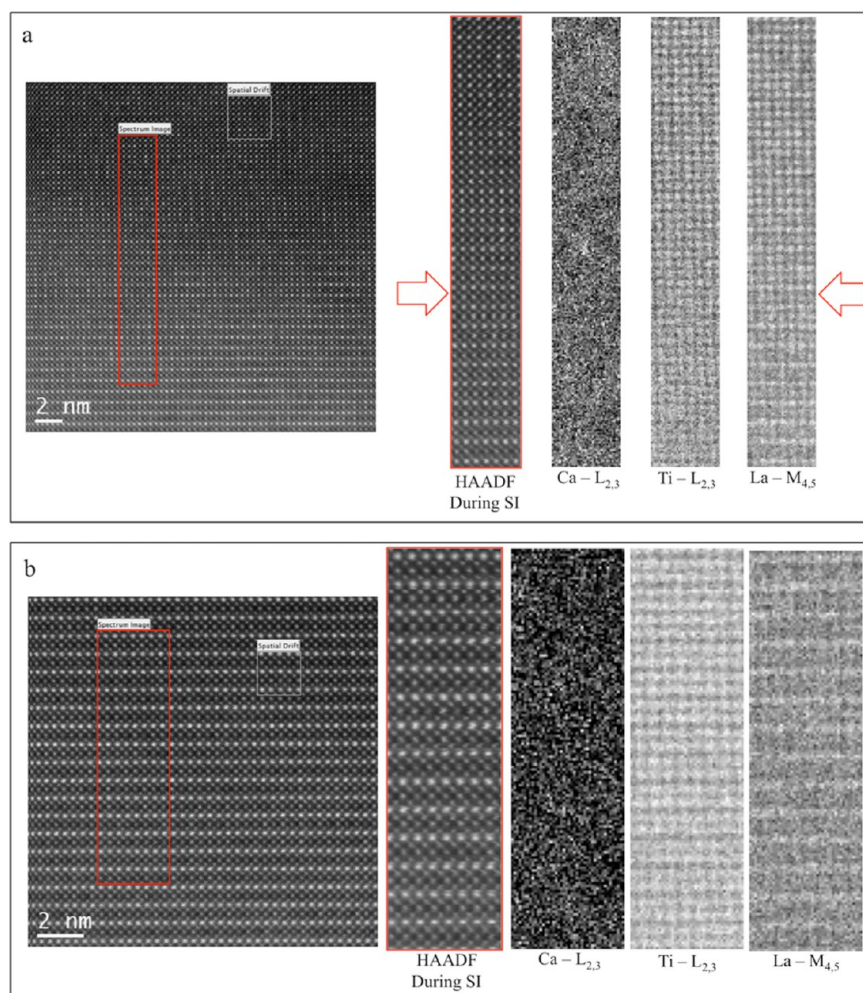


**Figure 8.** CLTO  $x = 0.9$  specimen (same particle as in Figure 9) along the  $[100]_p$  zone axis. (a) HAADF image of an area with transition from single perovskite structure (top half) to double-layered perovskite (bottom half—the arrows roughly point to the transition region); on the right, the HAADF signal gathered during SI acquisition and the raw elemental maps from corresponding characteristic edges. (b) HAADF image from an area with long-range ordering double-perovskite structure (left), with HAADF signal taken alongside SI and maps (right).

a finer spatial resolution. The spots marked in the STEM-DF image, with numbers 1 through 6, designate the locations of the probe corresponding to the CBED patterns shown in panel (c). Here, it can be observed that the appearance of the fractional diffraction peaks does not occur evenly across the domain structure within this grain. For instance, comparing #1, #2, and #3,  $1/2111$  peaks seem to be present in #2, but absent in cases of #1 and #3 (note arrows in #2). More drastically, this can be recognized for the case of patterns #4, #5, and #6, where the  $1/2001$  spot is strongly present in #5 and absent in the other two (arrowed). A lower intensity can also be discerned where  $1/21-10$  reflections are expected to be present. This clearly demonstrates that the TEM selected-area diffraction pattern (Figure 7(b)) is an averaged diffraction signal with contributions from all of the subdomains, averaged across the entire grain. STEM/CBED measurements show that each domain is associated with a slightly modified symmetry: with  $1/2001$  pointing toward doubling of the  $c$  axis and  $1/2111$  indicating deviation from  $a^-b^0c^0$  tilt system for the  $Cm\bar{m}m$  symmetry ( $Cm2m$  symmetry with  $a^-b^0c^+$  tilt could explain this superstructure reflection).<sup>34</sup> What is important to note here is the smaller scale, and consequently higher number density, of such domains compared to those observed earlier in low La-content CLTO samples (Figure 2).

For a more detailed analysis on the nature of the observed domains above, crushed powder samples were studied using aberration-corrected STEM/EELS. One CLTO  $x = 0.9$  particle oriented along the  $[100]_p$  zone axis, imaged using the HAADF detector, is shown in Figure 8. In the upper region of the HAADF image in panel (a), lines of higher intensity, distributed with no long-range ordering, are observed. Core-loss EELS spectrum imaging from a selected region, shown on the right-hand side of panel (a), indicates that the line formations with higher HAADF intensity are comprised of La-rich columns. The Ca signal is noisier than the La signal due to the proximity to the C–K edge (and resulting difficulties in obtaining a good background subtraction), but does not indicate any ordering. This regime was not persistent across the entire particle. In the lower half section of the same image, the “random” perovskite structure—this is not entirely random, given the presence of line clusters of La described above—transforms into a double perovskite structure, with doubling of the  $c$  axis. The La- $M_{4,5}$  map highlights this transition, with the upper half corresponding to the primitive pseudocubic perovskite unit cell and the lower half demonstrating condensation of La ions on alternating (001) planes, doubling the  $c$  axis in the cubic unit cell. The arrows beside the HAADF, acquired during spectrum imaging, and the La map point



roughly to where the transition takes place. Figure 8(b) shows an area away from the transition zone and entirely showing the double-perovskite ordering regime. Here the La- $M_{4,5}$  map, in confirmation of the observed HAADF intensity variations, shows a doubling of the primitive  $c$ -axis and preferential ordering of La ions and vacancies. It should be noted that the 001 planes with less intensity in the HAADF signal are not fully devoid of La, as is evidenced by the occasional high-intensity column on the vacancy-rich planes (also observed in the La map).

Within the particle above with long-range  $\text{La}^{3+}/\text{V}_{\text{Ca}}^{2-}$  ordering, twins were also encountered. Figure 9(a) and 9(b) are HAADF

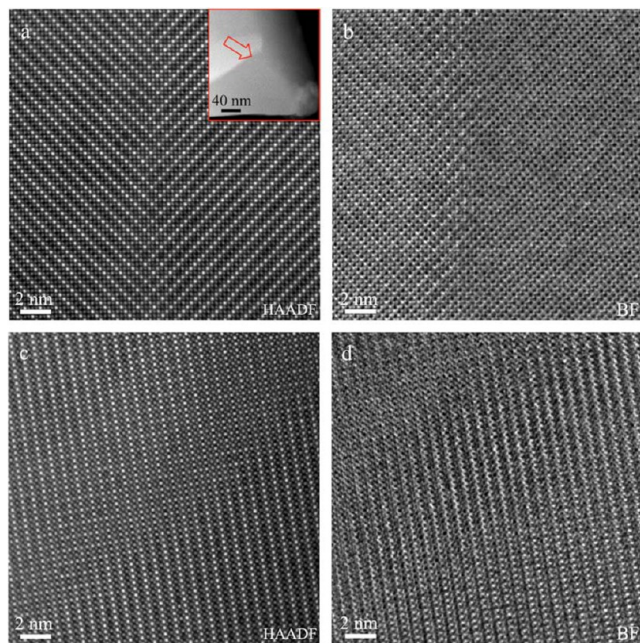


**Figure 9.** CLTO  $x = 0.9$  specimen (same particle and zone axis as the previous figure) (a) HAADF and (b) BF pair images showing a twin-like boundary. The inset in panel (a) shows the region with the twin at low magnification. (c and d) HAADF/BF image pair within the same particle showing another type of boundary between two double perovskite domains.

and BF pair images showing a twin boundary, with a low magnification view of the corresponding region presented as the inset in panel (a) (arrowed). The twin boundary corresponds to  $\sim 90^\circ$  rotation in the lattice ( $\sim 0.6^\circ$  deviation); hence, the twin can be identified as a  $90^\circ[100]_p$  tilt boundary. The core-loss EELS spectrum image, shown in the Supporting Information (Figure S7), confirms a direct correlation between the columns with high intensity to higher concentrations of La. Alongside this rotation in the double-perovskite structure, evident in the HAADF image, the BF signal indicates a change moving across the twin boundary. In the same particle, another boundary configuration of two meeting ordered double perovskite domains was observed. In this case, as shown in panels (c) and (d) in Figure 9 (pair HAADF/BF images), the La-rich planes in the first domain, upon passing through a transitional boundary, turn into vacancy-rich planes in the second domain and vice versa. This boundary can be identified as an  $180^\circ[100]_p$  tilt boundary.

In order to better resolve the changes in the octahedral tilts and investigate the ordering behavior of the vacancies at a different projection, STEM analysis was performed along the

$[110]_p$  zone axis of the  $Cm\bar{m}m$  structure, shown in Figure 10. In panel (a) the HAADF signal at relatively low magnification (20

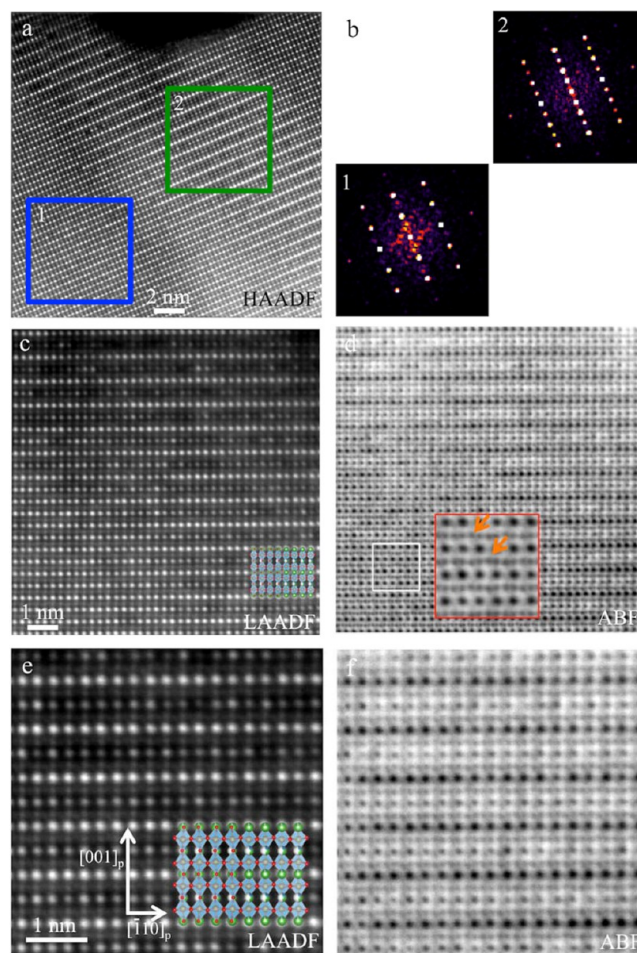


**Figure 10.** CLTO  $x = 0.9$ , along the  $[110]_p$  zone axis: (a) HAADF image with 20 nm FOV, (b) FFT from the marked regions in (a). (c and d) LAADF and ABF pairs at 10 nm FOV at the transition regions. (e and f) LAADF and ABF pairs at 5 nm FOV from the double perovskite domain. Crystal models are superimposed in panels (c) and (e). The inset in (d) is the detail of the marked area with white box on the left-hand side. [Color scheme in the crystal models: Ti orange, O red, Ca blue, and La green.]

nm field of view) shows an area, which includes both the “random” single unit cell perovskite structure and a highly ordered double perovskite region. Two regions, falling into the random and the ordered domains, are marked in (a), with corresponding FFTs shown in panel (b). It can be seen that  $1/2001_p$  peaks are present in the ordered region (#2) that are absent in the single perovskite domain (#1).

This observation is in-line with Figure 7, comparing point diffraction patterns #4, #5, and #6, with location corresponding to #5 marker having a double perovskite ordered structure. Similar bands of double perovskite domains were observed in the same particle as shown in Figure 10. Panels (c) and (d) present LAADF (low-angle annular dark-field)/ABF (annular bright-field) images highlighting the transition from a single to a double perovskite structure. High-magnification LAADF/ABF micrographs from the ordered domain, panels (e) and (f), point to variations in  $\text{La}^{3+}$  occupancy on the  $(001)_p$  planes. Crystal models along the same zone axis are superimposed in

panels (c) and (d), highlighting the feature of this zone axis that neighboring atomic planes, perpendicular to  $[001]_p$ , alternate between (Ca,La)/O planes and Ti/O planes. It can be observed in panel (f) that O sites within the double perovskite domain do not show deviation from the crystal model. In contrast, close inspection of the single perovskite region, highlighted area in panel (d), clearly shows distortions in the O lattice (examples marked by arrows). In order to accurately map the displacement of the cations along this zone axis, an HAADF image—after applying nonlinear scanning drift correction—was used, as shown in Figure 11(a). In panel (b), an averaged unit cell,

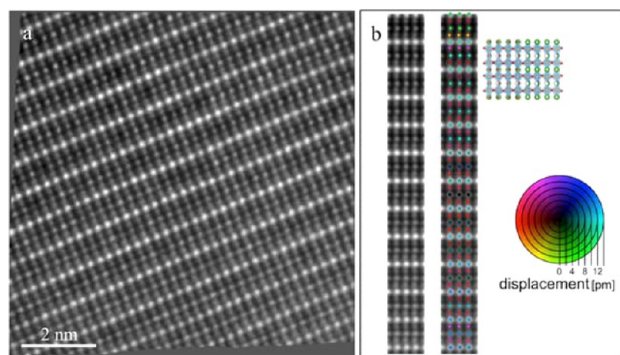


**Figure 11.** CLTO  $x = 0.9$ , along the  $[110]_p$  zone axis: (a) HAADF image after nonlinear scan drift correction, (b) averaged unit cell (left) and the displacement map (right) of the A and B-site cations. Legend for the magnitude and direction of the displacement is shown on the lower right. Crystal model along the same zone axis is presented for comparison.

based on the HAADF image, along with a displacement map of the cationic sites is presented. Compared to the crystal model along the same zone axis, it appears that the  $Ti^{4+}$  cations are displaced toward the left-hand side of the octahedral spaces. This observation is discussed in the following sections.

#### 4. DISCUSSION

Comparing the two extremes in La composition within  $Ca_{1-x}La_{2x/3}TiO_3$  perovskites, there is a strong tendency for the La-rich compositions to exhibit long-range vacancy ordering, while, on the La-lean side, large domains were identified with extended defect structures, some of which are tilt boundaries. Observation of boundaries that were more prominently visible in the BF signal, and less so in HAADF, was recurrent. Analysis of the A-site displacement, mapped using the HAADF signal, was essential in identifying the nature of these boundaries. Even though the presence of these boundaries was readily recognized in the BF image, due to sensitivity to both thickness and probe tilt, this signal was not suitable for quantifying atomic site positions. These boundaries proved to be tilt boundaries in all cases observed. In the  $Pbnm$  space group we have identified the following tilt boundaries:  $90^\circ[010]_p$  (twice) and  $90^\circ[001]_p$ . In the  $Pbnm$  case, identification of such boundaries was not trivial and required access to both HAADF and BF (or ABF) signals, whereas, for  $Cmnm$  symmetry, discussed below, the tilt boundary was readily evident in the HAADF signal, as is highlighted by change in the  $La^{3+}/V_{Ca}^{2-}$  ordering direction.

In the La-rich perovskite ( $x = 0.9$ ),  $Ca_{0.1}La_{0.6}TiO_3$ , long-range ordering in vacancies versus  $La^{3+}$  cations, with doubling of the  $[001]_p$  axis of the pseudocubic unit cell was observed, in

accordance with previous diffraction studies.<sup>19</sup> Our observations clearly demonstrate though that this doubling of the  $c_p$  axis cannot describe the entire microstructure. These double perovskite regions either emerge from regions with random vacancy distribution (as shown earlier, along both  $[100]_p$  and  $[110]_p$ ) or are separated from other double perovskite regions by tilt boundaries. In the  $Cmnm$  case, two of the following boundaries were observed:  $90^\circ[001]_p$  and  $180^\circ[001]_p$ . The boundaries within double perovskite domains were most prevalent in a FIB-prepared sample directly from the surface of the pellet. This could be due to higher vacancy concentrations closer to the surface, resulting in a higher number density of double-perovskite domains. Domains corresponding to octahedral tilt geometries different from the  $a^-b^0c^0$  system, anticipated for the  $Cmnm$  symmetry based on the structure proposed by Zhang et al.,<sup>19</sup> were also observed (i.e.,  $1/2111$  reflection observed in panel (c) of Figure 7). It is known that thermal history plays an important role in the appearance or suppression of long-range vacancy/cation ordering in A-site deficient perovskites, with fast cooling rates arresting the necessary diffusional processes conducive to such ordering.<sup>35,36</sup> Given that the specimens examined here share the same thermal history, it strongly indicates that the observed disparity in ordering behavior of  $V_{Ca}^{2-}/La^{3+}$  across the two ends of La compositions is a direct consequence of changes in chemistry.

A-site cation ordering in  $AA'BO_3$  perovskites, as observed for  $x = 0.9$  CLTO, is far less common than B-site cation ordering in  $ABB'O_3$  perovskites;<sup>37</sup> but if present, A-site ordering almost exclusively adopts a layered ordering configuration.<sup>38</sup> Some other cases of columnar A-site ordering,<sup>39</sup> or a complex interplay between microtwinning and columnar ordering,<sup>40</sup> have also been reported. The more prevalent layered ordering results in differences of environment for anions; that is, one-sixth of the anions are surrounded by four A cations while another one-sixth are surrounded by four A' cations. This bonding discrepancy is relieved, in perovskites with a highly charged  $d^0$  cation on the B-site like  $Ti^{4+}$ , most preferably by the displacement of B-site cation toward the A-site cation layer with higher concentration of vacancies (this is known as second order Jahn–Teller (SOJT) distortion).<sup>38,41</sup> In our observations along the  $[110]_p$  zone axis of the  $x = 0.9$  CLTO, mapping the cationic displacements as presented in Figure 11, a shift in the  $Ti^{4+}$  position toward the low occupancy  $(001)_p$  plane was not observed, indicating that the SOJT mechanism suggested above is not active in this perovskite. Instead, a lateral shift in Ti within the octahedral spaces is observed, Figure 11(b). *Ab initio* calculations are needed to investigate the energetic favorability of this distortion mechanism versus the SOJT distortion suggested in other perovskites.

Layered ordering at the La-rich end of the  $Ca_{1-x}La_{2x/3}TiO_3$  series has been observed in similar systems, e.g.  $Sr_{1-x}La_{2x/3}TiO_3$ ,<sup>42</sup> and also in  $La_{2/3}TiO_{3-\lambda}$ ,<sup>13</sup> with small oxygen deficiency ( $\lambda$  close to 0.007), as previously mentioned in the Introduction. A layered ordering is also suggested to be present in  $La_{2/3-x}Li_{3x}TiO_3$  (LLTO) and  $La_{1/3-x}Li_{3x}NbO_3$  (LLNO) perovskites, with La-rich and La-poor planes alternating along the  $[001]_p$  direction similar to the  $x = 0.9$  composition of CLTO.<sup>43–45</sup> A combination of *ab initio* and Monte Carlo simulations on  $Sr_{1-x}La_{2x/3}TiO_3$  suggests long-range ordering of the A-site as the contribution of vacant sites increases (larger  $x$  values).<sup>46</sup> According to this study, at low vacancy concentrations ( $V_{Sr}^{2-}$ ) the electrostatic affinity between  $La^{3+}$  and  $V_{Sr}^{2-}$

dominates and these form neutral arrangements, e.g. linear or bent trimers, to minimize energy. In the presence of high vacancy concentration, the strain energy, favoring columns of neighboring vacancies, outweighs the electrostatic interactions and leads to long-range ordering. This is suggested to arise from interplay between electrostatic forces (i.e., between  $\text{La}^{3+}$  and  $V_{\text{Ca}}^{2-}$ ) and strain energy, with the latter being dominant for the case of long-range ordering of vacancy-La pairs at large  $x$  values. Nominally, in the  $x = 0.2$  perovskite (with  $Pbnm$  symmetry) we expect around 7% vacancies on A sites, whereas, in  $x = 0.9$  this amounts to 30%. Similar arguments could potentially apply for the CLTO system. An alternative crystal structure proposed for  $\text{La}_{2/3}\text{TiO}_3$  entails layered ordering with 2 layers of high La occupancy and 1 layer of vacancy-rich configuration with  $I4/mmm$  symmetry and  $a = b = 3.856 \text{ \AA}$  and  $c = 24.6 \text{ \AA}$ .<sup>17</sup> Given our HAADF and EELS observations, we can safely rule out the occurrence of similar ordering in La-rich CLTO perovskite.

In  $x = 0.9$  CLTO, diffraction evidence was observed pointing to a modified tilting configuration, deviating from the  $a^-b^0c^0$  regime expected from  $Cmmm$  symmetry (Table 1), i.e. 1/2111 peak presence in Figure 7. A similar observation was reported for low Li-content  $\text{La}_{2/3-x}\text{Li}_x\text{TiO}_3$ ,<sup>47</sup> with the presence of the 1/2111 peak indicating rhombohedral symmetry, where prior diffraction data suggested  $Pm-3-$  and  $P4/mmm$  symmetries with no octahedral tilting and hence requiring the absence of a peak at the 1/2111 position. Regions with modified Ti–O tilting were shown to be responsible for this peak's presence. The same appears to be the case for  $x = 0.9$  CLTO, as shown in Figures 10(d) and 11(b), with evidence of distortions in O and Ti lattices giving rise to the 1/2111 peak. This is another aspect of the microstructure that was not detectable via volume-averaged diffraction measurements.<sup>19</sup>

A recent study on the similar A-site deficient perovskite system  $\text{Ca}_{0.1}\text{Nd}_{0.6}\text{TiO}_3$  observed an incommensurate superlattice structure.<sup>48</sup> Taking up a morphology described as “nanochessboard”, these domains were shown to correspond to strain arising from modulations in the octahedral tilting, and not from chemical segregation, as suggested in earlier studies on similar systems.<sup>49,50</sup> In  $\text{Nd}_{2/3-x}\text{Li}_x\text{TiO}_3$  perovskites, analogous features in the microstructure, i.e. one- or two-dimensional stripe patterns and nanochessboard arrangements, were correlated with parallel ordering and spinodal decomposition along different crystallographic directions.<sup>51</sup> Similar behavior was not encountered in CLTO. Instead, the common structural feature in both extreme cases of composition in CLTO appeared to be the development of tilt boundaries, as was documented throughout this study. The prevalence of twinning and twin-like boundaries in perovskites was recognized from the very early days of optical crystallography investigations of natural  $\text{CaTiO}_3$  minerals.<sup>52</sup> In the first detailed electron microscopy characterization of  $\text{CaTiO}_3$ , White et al. identified two types of tilt boundary systems (See Supporting Information, Figure S8, for conversion from reported  $Pcmm$  indices<sup>53</sup> to pseudocubic):<sup>54</sup>  $90^\circ$  and  $180^\circ$  rotation about the normal to  $(100)_p$ . The former case was one of the boundary types observed in the present study. Interestingly, the LLTO system also demonstrated a high number density of  $90^\circ$  rotation boundaries, varying in size depending on the composition.<sup>55</sup> Similarly, doubling of the unit cell along with appearance of twinning with  $90^\circ$  rotation of the lattice was reported in  $\text{LaAlO}_3$ -stabilized  $\text{La}_{2/3}\text{TiO}_3$ .<sup>56</sup> A follow-up study on this system linked a higher number density of twins to faster

cooling rates,<sup>57</sup> postulating that the occurrence of these defects points to a mechanism that accommodates the induced strains through the phase transformations. Although we have not investigated the effect of cooling rate on the twinning domains in CLTO, it is safe to infer the same trend. It is also possible that strain does not play a major role and we are observing the effect of change in space groups, modifying a crystallographic direction with high symmetry at elevated temperatures to a number of nonequivalent directions at a lower temperature, lower symmetry space group in neighboring domains. More work is required to unequivocally resolve the above distinction.

Since the tilt boundaries observed in CLTO are accommodated by subtle changes in the octahedral spaces, they were not accompanied by complex boundary structures, such as those reported for  $\text{SrTiO}_3$ .<sup>58,59</sup> In those cases, as the boundary structure involved repeating patterns of Sr and Ti, they were readily recognizable in the HAADF signal. A twin boundary in  $\text{CaTiO}_3$  in one experimental study was associated with polarization in Ti, with 3 to 6 pm deviation from the zero-polarity position,<sup>60</sup> pointing to a very localized ferroelectric domain with a nonpolar matrix. However, this was not observed in the boundaries examined here; namely, the polarization in Ti was close to or smaller than our peak position precision of 3 pm.

## 5. CONCLUSIONS

Ordering in the A-site occupancy and the nature of the domain boundaries were characterized in the  $\text{Ca}_{1-x}\text{La}_{2x/3}\text{TiO}_3$  perovskite structure using atomically resolved STEM/EELS analysis. In the low La-content regime, with  $Pbnm$  space group and examined along  $[010]_p$ ,  $[001]_p$ , and  $[110]_p$  zone axes, long-range ordering in  $\text{La}^{3+}$  or vacancies were not observed. Micrographs of the HAADF signal pointed to occasional linear configuration of  $\text{La}^{3+}$  ions. Tilt boundaries, with prominent contrast in BF images but almost invisible in the HAADF signal, were commonly observed. In this composition range, we identified the following tilt boundaries:  $90^\circ[010]_p$  (twice) and  $90^\circ[001]_p$ . Successful characterization of these boundaries was only possible through simultaneous access to both BF and HAADF signals, and applying a detailed peak-finding and displacement-mapping routine to the HAADF image.

At the La-rich end of the composition, with  $Cmmm$  space group and examined along the  $[100]_p$  and  $[110]_p$  zone axes, long-range ordering of vacancies and  $\text{La}^{3+}$  ions was observed. This was demonstrated with alternating La-rich and La-poor layers on  $(001)_p$  planes, effectively creating a double perovskite lattice along the  $c$  axis. These highly ordered domains were observed to be either isolated within a “matrix” of random distribution of vacancies/ $\text{La}^{3+}$ , or found with a high number density, covering nearly an entire particle. In regions with a high population of double perovskite domains, these ordered regions were separated from each other by tilt boundaries, with  $90^\circ$  or  $180^\circ$  misorientation across the two neighboring grains. Observation of the  $1/2111_p$  peak in the high-La-content CLTO electron diffraction patterns was correlated to regions with distortions in O–Ti bonds.

## ■ ASSOCIATED CONTENT

### Supporting Information

The Supporting Information is available free of charge on the ACS Publications website at DOI: 10.1021/acs.inorgchem.6b02087.

Second example of tilt boundary observed in  $x = 0.1$  CLTO. Low magnification images of the particles used for Figures 3, 4, 6, and 7 along with corresponding SAD patterns. Array of multislice simulations for BF and HAADF signals, CLTO  $x = 0.2$ , with changes in thickness and probe tilt. EELS map of area shown in Figure 9(a). Comparing  $Pbnm$  and  $Pcmm$  unit cells. (PDF)

## AUTHOR INFORMATION

### Corresponding Author

\*E-mail: [mohsen.danaie@materials.ox.ac.uk](mailto:mohsen.danaie@materials.ox.ac.uk), [danaie.mohsen@gmail.com](mailto:danaie.mohsen@gmail.com).

### Notes

The authors declare no competing financial interest.

## ACKNOWLEDGMENTS

Funding is acknowledged from the UK's Engineering and Physical Sciences Research Council (EPSRC) under grants EP/K029770/1 and EP/L005581/1. PDE acknowledges support from the U.S. Department of Energy, Office of Science, Fusion Energy Sciences. SML acknowledges funding from the EPSRC grant EP/G037140/1. SuperSTEM is the UK National Facility for Aberration-Corrected STEM, supported by EPSRC. Work at the Molecular Foundry was supported by the Office of Science, Office of Basic Energy Sciences, of the U.S. Department of Energy under Contract No. DE-AC02-05CH11231. Guidance in sample preparation from Amy Gandy is gratefully acknowledged.

## REFERENCES

- (1) Vashook, V.; Vasylechko, L.; Knapp, M.; Ullmann, H.; Guth, U. Lanthanum Doped Calcium Titanates: Synthesis, Crystal Structure, Thermal Expansion and Transport Properties. *J. Alloys Compd.* **2003**, *354*, 13–23.
- (2) Kim, I.-S.; Jung, W.-H.; Inaguma, Y.; Nakamura, T.; Itoh, M. Dielectric Properties of a-Site Deficient Perovskite-Type Lanthanum-Calcium-Titanium Oxide Solid Solution System [(1 - x)La<sub>2/3</sub>TiO<sub>3</sub> - xCaTiO<sub>3</sub> (0.1 ≤ x ≤ 0.96)]. *Mater. Res. Bull.* **1995**, *30*, 307–316.
- (3) Salje, E.; Zhang, H. Domain Boundary Engineering. *Phase Transitions* **2009**, *82*, 452–469.
- (4) Howard, C. J.; Lumpkin, G. R.; Smith, R. I.; Zhang, Z. Crystal Structures and Phase Transition in the System SrTiO<sub>3</sub>-La<sub>2/3</sub>TiO<sub>3</sub>. *J. Solid State Chem.* **2004**, *177*, 2726–2732.
- (5) Smith, K. L.; Lumpkin, G. R.; Blackford, M. G.; Colella, M.; Zaluzec, N. J. In Situ Radiation Damage Studies of La<sub>x</sub>Sr<sub>1-3x/2</sub>TiO<sub>3</sub> Perovskites. *J. Appl. Phys.* **2008**, *103*, 83531.
- (6) Ringwood, A. E.; Kesson, S. E.; Ware, N. G.; Hiberson, W.; Major, A. Immobilisation of High Level Nuclear Reactor Wastes in SYNROC. *Nature* **1979**, *278*, 219–223.
- (7) Ali, R.; Yashima, M. Space Group and Crystal Structure of the Perovskite CaTiO<sub>3</sub> from 296 to 1720 K. *J. Solid State Chem.* **2005**, *178*, 2867–2872.
- (8) Megaw, H. D. *Crystal Structures: A Working Approach*; Studies in physics and chemistry, no. 10; Saunders: Philadelphia; London, 1973.
- (9) Glazer, A. Simple Ways of Determining Perovskite Structures. *Acta Crystallogr., Sect. A: Cryst. Phys., Diffr., Theor. Gen. Crystallogr.* **1975**, *31*, 756–762.
- (10) Kestigian, M.; Ward, R. The Lanthanum-Titanium-Oxygen System. *J. Am. Chem. Soc.* **1955**, *77*, 6199–6200.
- (11) MacLean, D. A.; Ng, H.-N.; Greedan, J. E. Crystal Structures and Crystal Chemistry of the RETiO<sub>3</sub> Perovskites: RE = La, Nd, Sm, Gd, Y. *J. Solid State Chem.* **1979**, *30*, 35–44.
- (12) Eitel, M.; Greedan, J. E. A High Resolution Neutron Diffraction Study of the Perovskite LaTiO<sub>3</sub>. *J. Less-Common Met.* **1986**, *116*, 95–104.
- (13) Abe, M.; Uchino, K. X-Ray Study of the Deficient Perovskite. *Mater. Res. Bull.* **1974**, *9*, 147–155.
- (14) Inaguma, Y.; Liqun, C.; Itoh, M.; Nakamura, T.; Uchida, T.; Ikuta, H.; Wakihara, M. High Ionic Conductivity in Lithium Lanthanum Titanate. *Solid State Commun.* **1993**, *86*, 689–693.
- (15) MacChesney, J. B.; Sauer, H. A. The System La<sub>2</sub>O<sub>3</sub>-TiO<sub>5</sub>; Phase Equilibria and Electrical Properties. *J. Am. Ceram. Soc.* **1962**, *45*, 416–422.
- (16) Lee, H. J.; Park, H. M.; Cho, Y. K.; Nahm, S. Microstructure Characterization of the (1-x)La<sub>2/3</sub>TiO<sub>3</sub>-xLaAlO<sub>3</sub> System. *J. Am. Ceram. Soc.* **2003**, *86*, 1395–1400.
- (17) Gönen, Z. S.; Paluchowski, D.; Zavalij, P.; Eichhorn, B. W.; Gopalakrishnan, J. Reversible Cation/Anion Extraction from K<sub>2</sub>La<sub>2</sub>Ti<sub>3</sub>O<sub>10</sub>: Formation of New Layered Titanates, KLa<sub>2</sub>Ti<sub>3</sub>O<sub>9.5</sub> and La<sub>2</sub>Ti<sub>3</sub>O<sub>9</sub>. *Inorg. Chem.* **2006**, *45*, 8736–8742.
- (18) Vashook, V.; Vasylechko, L.; Trofimenko, N.; Kuznecov, M.; Otchik, P.; Zosel, J.; Guth, U. A-Site Deficient Perovskite-Type Compounds in the Ternary CaTiO<sub>3</sub>-LaCrO<sub>3</sub>-La<sub>2/3</sub>TiO<sub>3</sub> System. *J. Alloys Compd.* **2006**, *419*, 271–280.
- (19) Zhang, Z.; Lumpkin, G. R.; Howard, C. J.; Knight, K. S.; Whittle, K. R.; Osaka, K. Structures and Phase Diagram for the System CaTiO<sub>3</sub>-La<sub>2/3</sub>TiO<sub>3</sub>. *J. Solid State Chem.* **2007**, *180*, 1083–1092.
- (20) Aleksandrov, K. S.; Bartolomé, J. Structural Distortions in Families of Perovskite-like Crystals. *Phase Transitions* **2001**, *74*, 255–335.
- (21) Giannuzzi, L. A.; Stevie, F. A. A Review of Focused Ion Beam Milling Techniques for TEM Specimen Preparation. *Micron* **1999**, *30*, 197–204.
- (22) Pennycook, S. J.; Nellist, P. D. *Scanning Transmission Electron Microscopy: Imaging and Analysis*; Springer Science & Business Media: 2011.
- (23) Kim, Y.; Pennycook, S. J.; Kalinin, S. V.; Borisevich, A. Y.; Yu, P.; Ramesh, R.; Chu, Y. Direct Mapping of Octahedral Tilts in Perovskite Oxide Materials Using Bright Field Scanning Transmission Electron Microscopy. *Microsc. Microanal.* **2012**, *18* (Supplement S2), 420–421.
- (24) Zhu, Y.; Withers, R. L.; Bourgeois, L.; Dwyer, C.; Etheridge, J. Direct Mapping of Li-Enabled Octahedral Tilt Ordering and Associated Strain in Nanostructured Perovskites. *Nat. Mater.* **2015**, *14*, 1142–1149.
- (25) Aso, R.; Kan, D.; Shimakawa, Y.; Kurata, H. Octahedral Tilt Propagation Controlled by A-Site Cation Size at Perovskite Oxide Heterointerfaces. *Cryst. Growth Des.* **2014**, *14*, 2128–2132.
- (26) James, E. M.; Browning, N. D. Practical Aspects of Atomic Resolution Imaging and Analysis in STEM. *Ultramicroscopy* **1999**, *78*, 125–139.
- (27) Stadelmann, P. JEMS JAVA electron microscopy software; <http://www.jems-saas.ch/> (accessed Dec 17, 2015).
- (28) Ophus, C.; Ciston, J.; Nelson, C. T. Correcting Nonlinear Drift Distortion of Scanning Probe and Transmission Electron Microscopies from Image Pairs with Orthogonal Scan Directions. *Ultramicroscopy* **2016**, *162*, 1–9.
- (29) Kirkland, E. J. *Advanced Computing in Electron Microscopy*; Springer Science & Business Media: 2010.
- (30) Hitchcock, P. B.; Lappert, M. F.; Maron, L.; Protchenko, A. V. Lanthanum Does Form Stable Molecular Compounds in the + 2 Oxidation State. *Angew. Chem., Int. Ed.* **2008**, *47*, 1488–1491.
- (31) Shannon, R. D. Revised Effective Ionic Radii and Systematic Studies of Interatomic Distances in Halides and Chalcogenides. *Acta Crystallogr., Sect. A: Cryst. Phys., Diffr., Theor. Gen. Crystallogr.* **1976**, *32*, 751–767.
- (32) Woodward, D. L.; Reaney, I. M. Electron Diffraction of Tilted Perovskites. *Acta Crystallogr., Sect. B: Struct. Sci.* **2005**, *61*, 387–399.
- (33) Yamazaki, T.; Kawasaki, M.; Watanabe, K.; Hashimoto, I.; Shiojiri, M. Effect of Small Crystal Tilt on Atomic-Resolution High-Angle Annular Dark Field STEM Imaging. *Ultramicroscopy* **2002**, *92*, 181–189.

- (34) Kishida, K.; Goto, K.; Inui, H. Electron Diffraction of  $ABX_3$  Perovskites with Both Layered Ordering of A Cations and Tilting of  $BX_6$  Octahedra. *Acta Crystallogr., Sect. B: Struct. Sci.* **2009**, *65*, 405–415.
- (35) Howard, C. J.; Zhang, Z.; Carpenter, M. A.; Knight, K. S. Suppression of Strain Coupling in Perovskite  $La_{0.6}Sr_{0.1}TiO_3$  by Cation Disorder. *Phys. Rev. B: Condens. Matter Mater. Phys.* **2007**, *76*, 54108.
- (36) Labeau, M.; Grey, I. E.; Joubert, J. C.; Vincent, H.; Alario-Franco, M. A. Structural Studies on A-Cation-Deficient Perovskite-Related Phases. II. Microdomain Formation in  $ThNb_4O_{12}$ . *Acta Crystallogr., Sect. A: Cryst. Phys., Diffraction, Theor. Gen. Crystallogr.* **1982**, *38*, 753–761.
- (37) Davies, P. K. Cation Ordering in Complex Oxides. *Curr. Opin. Solid State Mater. Sci.* **1999**, *4*, 467–471.
- (38) King, G.; Woodward, P. M. Cation Ordering in Perovskites. *J. Mater. Chem.* **2010**, *20*, 5785–5796.
- (39) Aimi, A.; Mori, D.; Hiraki, K.; Takahashi, T.; Shan, Y. J.; Shirako, Y.; Zhou, J.; Inaguma, Y. High-Pressure Synthesis of A-Site Ordered Double Perovskite  $CaMnTi_2O_6$  and Ferroelectricity Driven by Coupling of A-Site Ordering and the Second-Order Jahn–Teller Effect. *Chem. Mater.* **2014**, *26*, 2601–2608.
- (40) Labeau, M.; Grey, I. E.; Joubert, J. C.; Chenevas, J.; Collomb, A.; Guitel, J. C. The Structure of the A-Cation-Deficient Perovskite  $UNb_4O_{12}$ . *Acta Crystallogr., Sect. B: Struct. Sci.* **1985**, *41*, 33–41.
- (41) Knapp, M. C.; Woodward, P. M. A-Site Cation Ordering in  $AA'BB'O_6$  Perovskites. *J. Solid State Chem.* **2006**, *179*, 1076–1085.
- (42) Howard, C. J.; Zhang, Z. Structures and Phase Transition in the Layered Perovskite  $La_{0.6}Sr_{0.1}TiO_3$ : A New Orthorhombic Structure Solved from High-Resolution Diffraction in Combination with Group Theoretical Analysis. *J. Phys.: Condens. Matter* **2003**, *15*, 4543.
- (43) Catti, M. Ion Mobility Pathways of the  $Li^+$  Conductor  $Li_{0.125}La_{0.625}TiO_3$  by Ab Initio Simulations. *J. Phys. Chem. C* **2008**, *112*, 11068–11074.
- (44) Gao, X.; Fisher, C. A. J.; Ikuhara, Y. H.; Fujiwara, Y.; Kobayashi, S.; Moriwake, H.; Kuwabara, A.; Hoshikawa, K.; Kohama, K.; Iba, H.; Ikuhara, Y. Cation Ordering in A-Site-Deficient Li-Ion Conducting Perovskites  $La_{(1-x)/3}Li_xNbO_3$ . *J. Mater. Chem. A* **2015**, *3*, 3351–3359.
- (45) García-Martín, S.; Alario-Franco, M. A.; Ehrenberg, H.; Rodríguez-Carvajal, J.; Amador, U. Crystal Structure and Microstructure of Some  $La_{2/3-x}Li_{3x}TiO_3$  Oxides: An Example of the Complementary Use of Electron Diffraction and Microscopy and Synchrotron X-Ray Diffraction To Study Complex Materials. *J. Am. Chem. Soc.* **2004**, *126*, 3587–3596.
- (46) Thomas, B. S.; Marks, N. A.; Harrowell, P. Inversion of Defect Interactions due to Ordering in  $Sr_{1-3x/2}La_xTiO_3$  Perovskites: An Atomistic Simulation Study. *Phys. Rev. B: Condens. Matter Mater. Phys.* **2006**, *74*, 214109.
- (47) García-González, E.; Urones-Garrote, E.; Várez, A.; Sanz, J. Unravelling the Complex Nanostructure of  $La_{0.5-x}Li_{0.5-x}Sr_{2x}TiO_3$  Li Ionic Conductors. *Dalton Trans.* **2016**, *45*, 7148–7157.
- (48) Azough, F.; Kepaptsoglou, D.; Ramasse, Q. M.; Schaffer, B.; Freer, R. On the Origin of Nano-chessboard Superlattices in A-Site-Deficient Ca-Stabilized  $Nd_{2/3}TiO_3$ . *Chem. Mater.* **2015**, *27*, 497–507.
- (49) Guiton, B. S.; Davies, P. K. Nano-Chessboard Superlattices Formed by Spontaneous Phase Separation in Oxides. *Nat. Mater.* **2007**, *6*, 586–591.
- (50) Withers, R. L.; Bourgeois, L.; Snashall, A.; Liu, Y.; Norén, L.; Dwyer, C.; Etheridge, J. Chessboard/Diamond Nanostructures and the A-Site Deficient,  $Li_{1/2-3x}Nd_{1/2+x}TiO_3$ , Defect Perovskite Solid Solution. *Chem. Mater.* **2013**, *25*, 190–201.
- (51) Lu, J. B.; Yang, H. X.; Li, Z. A.; Ma, C.; Shi, H. L.; Zeng, L. J.; Li, J. Q. Phase Separation, Cation Ordering and Nano-Structural Complexities in  $Nd_{2/3-x}Li_{3x}TiO_3$  with  $x = 0.14$ . *J. Solid State Chem.* **2008**, *181*, 3194–3199.
- (52) Bowman, H. L. On the Structure of Perovskite from the Burgumer Alp, Pfitschthal, Tyrol. *Mineral. Mag.* **1908**, *15*, 156–176.
- (53) Kay, H. F.; Bailey, P. C. Structure and Properties of  $CaTiO_3$ . *Acta Crystallogr.* **1957**, *10*, 219–226.
- (54) White, T. J.; Segall, R. L.; Barry, J. C.; Hutchison, J. L. Twin Boundaries in Perovskite. *Acta Crystallogr., Sect. B: Struct. Sci.* **1985**, *41*, 93–98.
- (55) Fourquet, J. L.; Duroy, H.; Crosnier-Lopez, M. P. Structural and Microstructural Studies of the Series  $La_{2/3-x}Li_{3x}TiO_3$ . *J. Solid State Chem.* **1996**, *127*, 283–294.
- (56) Azough, F.; Wang, W.; Freer, R. The Crystal Structure of  $LaAlO_3$ -Stabilized  $La_{2/3}TiO_3$  Ceramics: An HRTEM Investigation. *J. Am. Ceram. Soc.* **2009**, *92*, 2093–2098.
- (57) Azough, F.; Freer, R.; Schaffer, B. Direct Observation of A-Site Vacancies and a Twin Boundary Structure in  $La_{2/3}TiO_3$ -Based Ceramics Using HAADF/STEM. *J. Am. Ceram. Soc.* **2010**, *93*, 1237–1240.
- (58) Browning, N. D.; Pennycook, S. J.; Chisholm, M. F.; McGibbon, M. M.; McGibbon, A. J. Observation of Structural Units at Symmetric [001] Tilt Boundaries in  $SrTiO_3$ . *Interface Sci.* **1995**, *2*, 397–423.
- (59) Browning, N. D.; Pennycook, S. J. Direct Experimental Determination of the Atomic Structure at Internal Interfaces. *J. Phys. D: Appl. Phys.* **1996**, *29*, 1779.
- (60) Van Aert, S.; Turner, S.; Delville, R.; Schryvers, D.; Van Tendeloo, G.; Salje, E. K. H. Direct Observation of Ferrielectricity at Ferroelastic Domain Boundaries in  $CaTiO_3$  by Electron Microscopy. *Adv. Mater.* **2012**, *24*, 523–527.